Chemical Science

ROYAL SOCIETY OF CHEMISTRY

EDGE ARTICLE

View Article Online
View Journal | View Issue

Cite this: *Chem. Sci.*, 2026, **17**, 3605

All publication charges for this article have been paid for by the Royal Society of Chemistry

Biomineralization-mimicking cooperative assembly for tailoring anisotropic hierarchically porous metal–organic frameworks

Ruigang Sun,[a] Ji Han,[a] Bin Zhao,[a] Bohan Liu,[a] Guangrui Chen,[ab] Haidong Xu,[a] Baiqi Wang,[a] Yanjing Gao,[a] Song Lin Zhang,[c] Yusuke Yamauchi,[def] Xiaoxin Chen*[a] and Buyuan Guan *[ab]

Anisotropic hierarchically porous metal–organic frameworks (MOFs) with asymmetric morphologies hold great promise for improving the utilization efficiency of the MOF matrix, thereby expanding their applicability. However, imparting MOFs with precisely controlled porous architectures and morphologies remains challenging. Here, an ingenious soft/hard matter phase transition co-mediated assembly strategy is developed to mimic the biomineralization process for synthesizing anisotropic UiO-66-NH_2 mesoporous nanobowls (UiO-66-NH_2 mesoNBs). This process relies on *in situ* generated amorphous lamellar anionic surfactant/Zr-oxo cluster complexes as metal sources and templates. This is followed by the slow decomposition of complexes and the co-assembly of ternary mixed micelles and MOF precursors on their surfaces, creating crystalline UiO-66-NH_2 mesoNBs with cylindrical mesochannels. The phase transition from lamellar to cylindrical mesophases is co-driven by changes in the packing parameters caused by the "soft" surfactant reorganization and variations in the charge density of the "hard" framework during crystallization from amorphous Zr-oxo clusters to the crystalline MOF matrix. By varying the surfactant ratios, UiO-66-NH_2 can form diverse novel nanostructures and achieve well-tailored pore sizes within the small mesoporous range. This work provides fundamental insights into the transformation processes in amphiphilic molecule-directed MOF biomimetic mineralization and offers a promising strategy for constructing anisotropic hierarchically porous MOFs with high structural tunability.

Received 2nd September 2025
Accepted 10th November 2025

DOI: 10.1039/d5sc06744h

rsc.li/chemical-science

Introduction

Metal–organic frameworks (MOFs), an important class of modular porous materials constructed from periodically linked inorganic metal ions/clusters and organic linkers, have attracted considerable interest across diverse fields owing to their highly tunable structures and compositions, large surface areas, and ultrahigh porosities.[1–6] However, their internal matrix is underutilized owing to their inherent microporosities and closed bulk structures. Over the past decade, substantial efforts have been devoted to optimizing their pore structures and controlling their morphologies to fully exploit their potential.[7–11] In recent years, anisotropic hierarchically porous materials, especially those with nanostructures that break centrosymmetry, have resulted in widespread and cross-disciplinary applications such as sensor devices, catalytic conversion, energy storage, and drug delivery vehicles.[12–16] This is because their asymmetric nanoarchitectures, multimodal pore structures, and high surface areas collectively increase the accessible surface area and enhance the mass transport efficiency, thereby improving the overall framework utilization efficiency of functional materials. Therefore, the development of new synthetic strategies to engineer MOFs with finely controllable hierarchical pore structures and asymmetric morphologies is expected to open new opportunities and broaden their applicability in a wide array of critical fields, such as catalysis, energy conversion, and biomedicine.

Bioinspired morphogenesis enables precise fabrication of materials featuring controlled sizes, morphologies, and architectures for tailored properties.[17–20] As a pivotal example, mimicking biomineralization typically involves two stages: (i) the "soft" organic matrix initially serves as a flexible template, directing inorganic mineral deposition and facilitating the

[a]*State Key Laboratory of Inorganic Synthesis and Preparative Chemistry, College of Chemistry, Jilin University, Qianjin Street 2699, Changchun 130012, P. R. China. E-mail: chenxiaoxin@jlu.edu.cn; guanbuyuan@jlu.edu.cn*

[b]*International Center of Future Science, Jilin University, Qianjin Street 2699, Changchun 130012, P. R. China*

[c]*Institute of Materials Research and Engineering (IMRE), Agency for Science, Technology and Research (A*STAR), 2 Fusionopolis Way, Singapore 138634, Singapore*

[d]*Australian Institute for Bioengineering and Nanotechnology (AIBN), The University of Queensland, Brisbane, QLD 4072, Australia*

[e]*Department of Materials Process Engineering, Graduate School of Engineering, Nagoya University, Furo-cho, Chikusa-ku, Nagoya, Aichi, 464-8603, Japan*

[f]*Department of Chemical and Biomolecular Engineering, Yonsei University, 50 Yonseiro, Seodaemun-gu, Seoul 03722, Republic of Korea*

formation of controlled porous structures;[21,22] (ii) intermediate metastable amorphous minerals undergoes further reactions including dissolution–recrystallization, aggregation, and phase transformation, which allows for controlling the morphogenesis of thermodynamically stable "hard" minerals.[23] By mimicking the biomineralization, diverse anisotropic hierarchically porous functional materials (*e.g.* porous filaments, porous nanosheets, three-dimensional lamellar porous structures, *etc.*) with controlled pore size and morphology have been achieved.[24–27] However, such strategies have scarcely been leveraged to regulate the structural features of MOFs, particularly their pore architecture and morphology. A primary challenge lies in the limited precision of pore size modulation achieved with organic species, typically modulators or surfactant porogens with limited functions, used for MOF synthesis.[28,29] Another significant obstacle lies in the absence of an in-depth understanding of the relevant formation mechanisms, which in turn poses great difficulty in collaboratively implementing precise control over two critical stages during the reaction process: the formation of metastable amorphous intermediates and the subsequent interfacial nucleation and growth of MOFs on these amorphous precursors. The above limitations severely hinder the ability to direct morphological evolution of MOFs through precursor-mediated transformations.[30,31] Therefore, achieving exquisite fabrication of anisotropic hierarchically porous MOFs with highly tunable pore structures and nanoarchitectures in a biomineralization-mimicking manner remains a significant challenge.

Herein, we demonstrate a soft/hard matter phase transition co-mediated assembly strategy that mimics the biomineralization process to synthesize anisotropic UiO-66-NH_2 mesoporous nanobowls (denoted as UiO-66-NH_2 mesoNBs) with finely tunable small mesopores. The involved self-assembly and phase transition processes are tracked using time-dependent small-angle X-ray scattering (SAXS), wide-angle X-ray diffraction (XRD), and transmission electron microscopy (TEM). Furthermore, the in-depth formation mechanism is comprehensively elucidated. This novel strategy hinges on the design and construction of metastable amorphous sodium dodecyl sulfate (SDS)/Zr-oxo cluster complexes with a lamellar mesophase, driven by strong coordination between SDS and Zr-oxo clusters. Subsequently, the *in situ* slow decomposition of these complexes releases SDS surfactants and Zr-oxo clusters. Concurrently, SDS, octadecyl dimethyl betaine (ODMB), and block copolymer F127 form mixed micelles that co-assemble with Zr-oxo clusters and organic ligands into cylindrical mesostructured UiO-66-NH_2 composites. These composites grow on the decomposing SDS/Zr-oxo cluster complexes, leading to the formation of crystalline anisotropic bowl-shaped MOFs with cylindrical mesochannels (Fig. 1a). Changes in the packing parameters caused by the formation of "soft" micelles assembled by three different surfactants, along with variations in the charge density of "hard" frameworks during crystallization from amorphous non-crosslinked Zr-oxo clusters to the crystalline MOF matrix, are crucial driving forces in altering the micellar curvature and inducing mesophase transition. Moreover, by varying the surfactant ratios, several novel nanostructures can be synthesized, such as hollow mesoporous particles with mesoNBs as subunits and mesoporous bowls with cracks near the opening, along with precise and continuous modulation of small mesopore sizes ranging from 2.65 to 6.80 nm. To highlight the structural advantages of UiO-66-NH_2 mesoNBs, they are further transformed into iron/nitrogen-doped carbon mesoporous nanobowls (Fe–N–C mesoNBs) through chemical vapor deposition (CVD) followed by chemical etching and these Fe–N–C mesoNBs exhibit efficient oxygen reduction reaction (ORR) performance with a half-wave potential of 0.89 V. Meanwhile, finite element simulations demonstrate that the unique bowl-shaped mesoporous structure can accelerate the mass transfer process, thereby significantly enhancing the three-phase interface reaction. The present work provides fundamental insights into the MOF biomimetic mineralization processes and offers a promising strategy for controlling complex pathways to precisely fabricate anisotropic hierarchically porous MOFs with high structural tunability.

Results and discussion

Structure of UiO-66-NH_2 mesoNBs

An overview scanning electron microscopy (SEM) image of the UiO-66-NH_2 mesoNBs reveals their uniform anisotropic bowl-shaped morphology with an average diameter of ~120 nm (Fig. 1b). Each bowl-shaped MOF nanoparticle is found to have a groove. As shown in the TEM image, numerous uniform and open pores can be observed within the bowl-shaped MOF nanoparticles (Fig. 1c). Close observation of the anisotropic bowl-like nanoparticle at higher magnification (Fig. 1d) reveals radially oriented cylindrical mesopores with an average pore size of ~4 nm running throughout the entire bowl. This pore structure could enhance the mass transport efficiency and increase the accessible surface area, thereby improving the overall utilization efficiency of the MOF's internal matrix. A series of tomographic TEM images with different facing directions from −40° to 40° is further used to observe a single UiO-66-NH_2 mesoporous nanobowl (Fig. 1e and S1). The corresponding elemental mapping images demonstrate a uniform distribution of C, N, and Zr within the as-synthesized UiO-66-NH_2 mesoNBs (Fig. 1f). XRD analysis confirms the crystallographic structure and phase purity of the resultant UiO-66-NH_2 mesoNBs. As shown in Fig. 1g, the diffraction peaks of UiO-66-NH_2 mesoNBs match well with those of UiO-66-NH_2 microporous crystals (UiO-66-NH_2 microCs, Fig. S2). Distinct from the type I isotherms observed for conventional UiO-66-NH_2 microCs, the N_2 sorption isotherms for the UiO-66-NH_2 mesoNBs display type IV curves with a hysteresis loop (Fig. 1h), indicating the presence of mesopores within the UiO-66-NH_2 mesoNBs. The Brunauer–Emmett–Teller (BET) surface areas of UiO-66-NH_2 mesoNBs and UiO-66-NH_2 microCs are calculated to be 667 $m^2 g^{-1}$ and 818 $m^2 g^{-1}$, respectively (Table S1). The reduced BET surface area of UiO-66-NH_2 mesoNBs compared to that of UiO-66-NH_2 microCs is attributable to the structural defects formed following the removal of the soft template in the MOF matrix. As anticipated, both samples exhibit similar micropore diameters determined using non-local density functional theory (NLDFT,

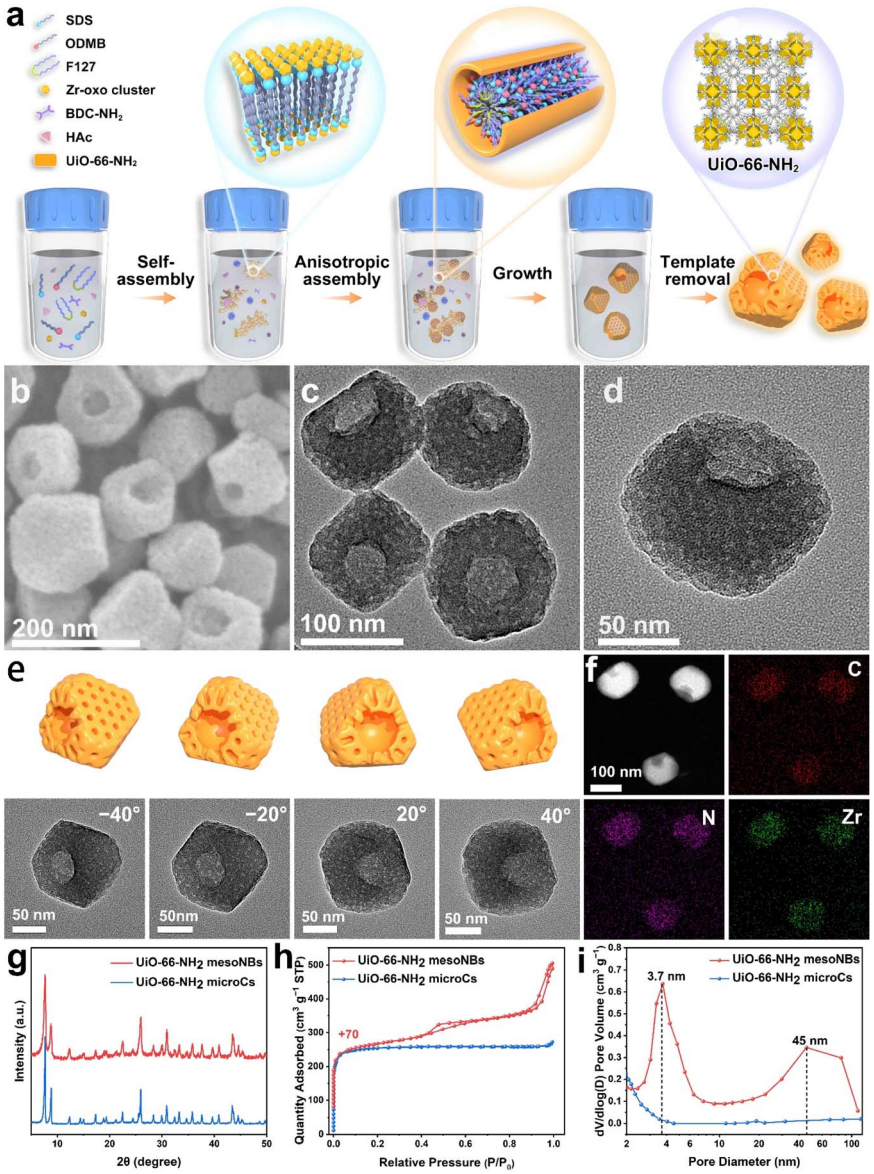

Fig. 1 Morphological and structural characterization of the UiO-66-NH_2 mesoNBs. (a) Schematic illustration of the synthetic protocol of the UiO-66-NH_2 mesoNBs. (b) SEM image, (c and d) TEM images, (e) schematic models and their corresponding tomographic TEM images, and (f) scanning transmission electron microscopy (STEM) image and elemental mapping images of UiO-66-NH_2 mesoNBs. (g) XRD patterns, (h) N_2 sorption isotherms, and (i) BJH pore size distributions of UiO-66-NH_2 mesoNBs and UiO-66-NH_2 microCs.

Fig. S3). According to the Barrett–Joyner–Halenda (BJH) model, the pore size distribution analysis of UiO-66-NH_2 mesoNBs reveals two distinct peaks centered at 3.7 and 45 nm (Fig. 1i), which can be attributed to the uniform small mesopores and the bowl opening in the anisotropic bowl-like MOF nanoparticles.

Soft/hard matter phase transition during self-assembly

The formation of UiO-66-NH_2 mesoNBs is mainly based on the initial construction of metastable SDS/Zr-oxo cluster complexes and precise control over the subsequent interface anisotropic assembly of the mesostructured SDS/ODMB/F127–UiO-66-NH_2 nanocrystals on the slowly decomposing SDS/Zr-oxo cluster templates. It is noteworthy that the strong coordination of the surfactant template SDS with Zr-oxo clusters promotes the formation of coral-like lamellar mesophase complexes. The complex assembly dynamics of SDS/ODMB/F127 mixed micelles with Zr-based MOF precursors, composed of Zr-oxo clusters and the organic ligand 2-aminoterephthalic acid (BDC-NH_2), subsequently drive the transformation of coral-like SDS/Zr-oxo cluster complexes into bowl-shaped SDS/ODMB/F127–UiO-66-NH_2 nanostructures.

This process is accompanied by a “soft” micelle structure transition from a lamellar to a cylindrical mesophase and a “hard” framework transformation from amorphous non-crosslinked Zr-oxo clusters to a crystalline MOF matrix. To

elucidate the formation process of UiO-66-NH_2 mesoNBs, time-dependent SAXS, wide-angle XRD, and TEM measurements were conducted by quenching the growth of the MOF reaction mixture at different time intervals. Initially, the rapid formation of complexes between SDS and Zr-oxo clusters occurs within minutes. The SAXS pattern (Fig. 2a) of the SDS/Zr-oxo cluster complexes exhibits two peaks at $q = 1.7$ and $2q$, suggesting the presence of an ordered lamellar structure (interlayer spacing 3.6 nm), as corroborated by the TEM image (Fig. 2c). Low magnification TEM shows that SDS/Zr-oxo cluster complexes exhibit a coralloidal morphology (Fig. S4). The wide-angle XRD pattern (Fig. 2b) indicates the amorphous nature of SDS/Zr-oxo cluster complexes. To analyze their composition, the complexes were dissolved in a solution of acetic acid and methanol and subjected to electrospray ionization-mass spectroscopy (ESI-MS). The results confirm the presence of Zr_6-oxo clusters and the dodecyl sulfate anion, indicating that no crosslinking occurs between the Zr_6-oxo clusters to form zirconia (Fig. S5). When the reaction time is extended to 10 hours, the decrease in SAXS peak intensity indicates the gradual decomposition of lamellar mesostructured SDS/Zr-oxo cluster complexes, while the narrowing and increased intensity of XRD peaks signifies the formation of UiO-66-NH_2. The TEM image (Fig. 2d) reveals the formation of mesostructured UiO-66-NH_2 nanocrystals with a diameter of about 90 nm on the surface of the SDS/Zr-oxo cluster complexes. This confirms that the SDS/Zr-oxo cluster complexes act as templates for the island nucleation and growth of mesostructured UiO-66-NH_2 particles. With a further increase in reaction time to 12 h, the continued loss of the lamellar mesostructure is evidenced by the further reduction of the (001) peak and the disappearance of the (002) peak in SAXS patterns, while a further increase in XRD peak intensity reflects the improved crystallinity of the Zr-based MOF. As shown in the TEM image (Fig. 2e), the diameter of the mesostructured UiO-66-NH_2 increases to 120 nm with the formation of bowl-like openings, while most of the lamellar mesophase SDS/Zr-oxo

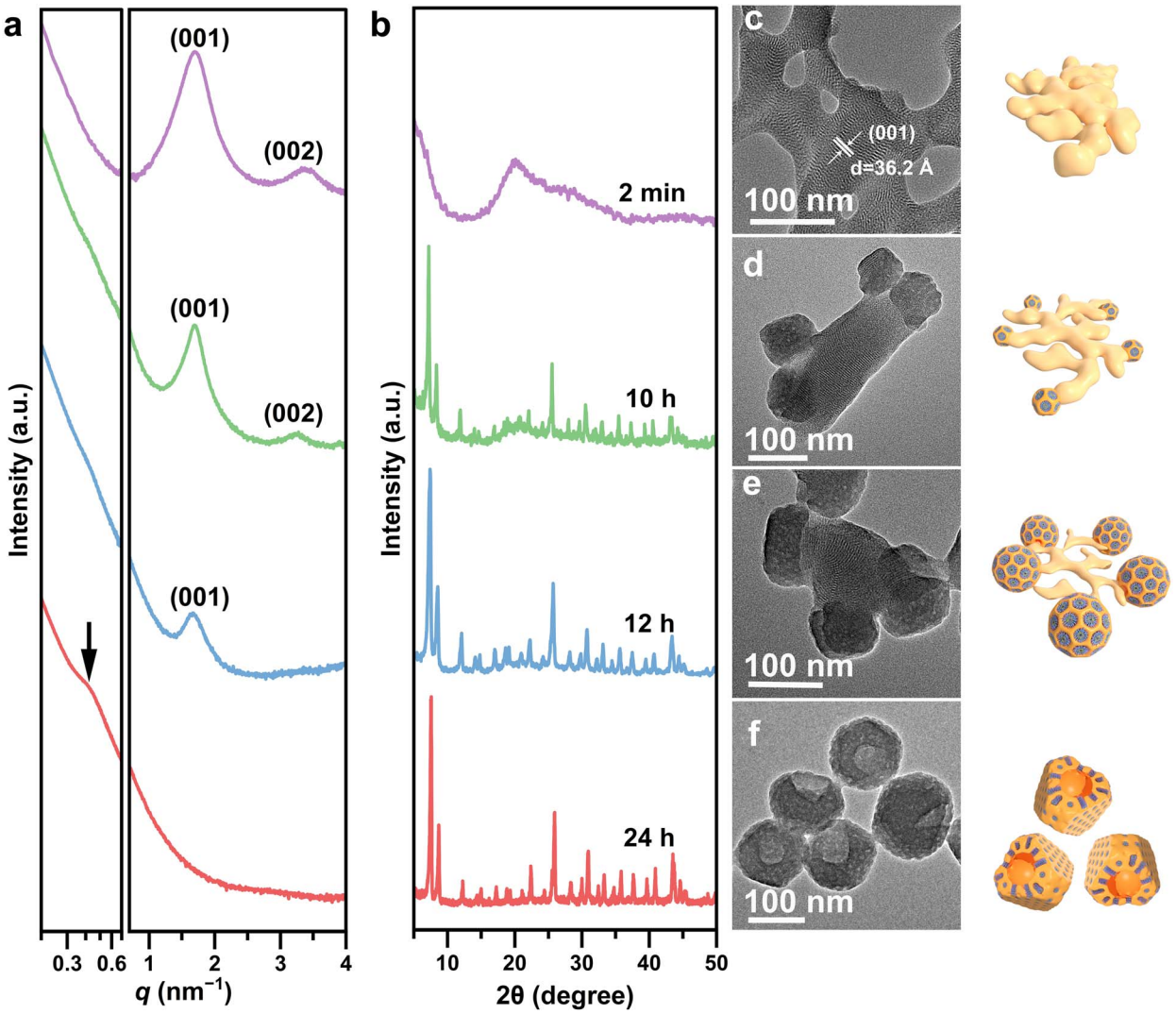

Fig. 2 Time-dependent characterization of the formation process of UiO-66-NH_2 mesoNBs. Time-dependent (a) SAXS patterns, (b) XRD patterns, and (c–f) TEM images, and representative 3D models of products obtained after 2 minutes, 10, 12, and 24 hours during the formation of UiO-66-NH_2 mesoNBs.

cluster complexes disappear (Fig. S6), indicating that the SDS/Zr-oxo cluster complexes decompose, thereby supplying components for the growth of the mesostructured UiO-66-NH_2. After 24 hours of reaction, the lamellar mesophase SDS/Zr-oxo cluster complexes completely disappear and well-defined UiO-66-NH_2 mesoNBs with cylindrical pores become visible (Fig. 2f), reflecting the soft matter mesophase transition from the initial lamellar mesophase to the cylindrical mesophase. A weak peak at $q = 0.4$ nm^{-1} in SAXS represents the short-range ordering of the mesopores in the UiO-66-NH_2 mesoNBs. The complete disappearance of the broad peak of amorphous SDS/Zr-oxo cluster complexes in the 13–25° range confirms the successful phase transition from non-crosslinked Zr-oxo clusters to crystalline UiO-66-NH_2 *via* solid framework crystallization.

To investigate the effects of different surfactants on the formation of asymmetric mesoporous MOF nanostructures, a series of control experiments are conducted. The UiO-66-NH_2 particles synthesized with only SDS surfactant (SDS-UiO-66-NH_2) possess a bowl-like morphology (Fig. S7a), further confirming the role of SDS/Zr-oxo cluster complexes as templates for MOF island nucleation and growth. However, it is noteworthy that the pore size of UiO-66-NH_2 prepared with SDS templates (Fig. S7b) is significantly smaller than that of the UiO-66-NH_2 mesoNBs (Fig. 1d). This suggests that the micelles involved in the formation of UiO-66-NH_2 mesoNBs are not composed solely of SDS surfactants. A possible explanation is that SDS and the block copolymer F127 with much longer hydrophobic chains than SDS and ODMB form larger mixed micelles when cooperatively self-assembled with the UiO-66-NH_2 precursor. However, the UiO-66-NH_2 nanoparticles (Fig. S8) produced through the co-assembly of SDS and F127 with UiO-66-NH_2 precursors exhibit a significantly smaller mesopore size than that of UiO-66-NH_2 mesoNBs (Fig. 1d), similar to the small pore size of UiO-66-NH_2 particles synthesized with SDS as a sole soft template (Fig. S7). This implies that SDS dominates the cooperative self-assembly process when F127 and SDS are co-assembled with UiO-66-NH_2 precursors. The reason may be that the interaction between F127 and Zr-oxo clusters is significantly weaker than that between SDS and Zr-oxo clusters, which is further confirmed by turbidity measurements of the reaction mixture upon directly mixing SDS and F127 with Zr-oxo clusters, respectively (Fig. S9 and S10). The addition of ODMB is crucial to enhance the interaction between SDS and F127 to achieve larger mesopores in UiO-66-NH_2. ODMB, when protonated under acidic conditions in the reaction system, could act as a cationic surfactant and form mixed micelles with the anionic surfactant SDS through strong electrostatic interactions.[32,33] Moreover, the nonionic surfactant F127 can be absorbed into the hydrophobic core of anionic–cationic mixed micelles through their hydrophobic ends, thereby reducing the bending elasticity of the mixed micelles.[34] Thus, the ODMB surfactant can be considered as a bridge, enhancing the interactions between F127 and SDS to form mixed micelles. As confirmed by Fourier transform infrared spectroscopy (FTIR) analysis, ternary mixed micelles co-assemble with Zr-oxo clusters and BDC-NH_2 into mesostructured SDS/ODMB/F127–Zr-based UiO-66-NH_2 composites (Fig. S11).

Based on the above results and analyses, we propose a scheme to illustrate the evolution pathway of anisotropic UiO-66-NH_2 mesoNBs (Fig. 3). In our synthesis, the formation of UiO-66-NH_2 mesoNBs is governed by the assembly of multiple amphiphilic surfactants and a MOF crystallization co-driven transformation process. The reorganization of surfactants and the crystallization of the MOF collectively account for the mesophase transition of the "soft" micelle from a lamellar to a cylindrical structure, as well as the transformation of the "hard" framework from amorphous non-crosslinked Zr-oxo clusters to crystalline UiO-66-NH_2. From the perspective of surfactant reorganization, the micellar structure can be guided by the surfactant packing parameter (g), which is defined in eqn (1)

$$g = \frac{v}{a_{0l_c}} \quad (1)$$

where v denotes the volume of the hydrophobic block, l_c signifies the hydrophobic tail length, and a_0 indicates the polar head surface area. For the block copolymer surfactant, g is mainly determined by the hydrophobic/hydrophilic ratio, namely, the V_H/V_L value (where V_H and V_L are the hydrophobic chain and hydrophilic chain volume fractions, respectively). Generally, different g values can impart distinct surface mean curvatures to the micelles, leading to the formation of diverse micellar structures.[35] Due to the g value of SDS being about 1 and its strong coordination with Zr-oxo clusters, the SDS surfactants and Zr-oxo clusters first co-assemble (*ca.* minutes) into non-crosslinked amorphous SDS/Zr-oxo cluster mesophases with MCM-50-like lamellar mesostructures, which act as metal sources and hard/soft templates for nucleating and growing mesoporous MOF nanobowls. As organic ligand BDC-NH_2 could coordinate strongly with the Zr-oxo clusters to form stable Zr-based MOFs, SDS/Zr-oxo cluster complexes dissolve slowly in the aqueous solution containing BDC-NH_2. Under acidic conditions, protonated ODMB and released SDS easily mix through strong electrostatic interactions. Simultaneously, F127 can be absorbed into the hydrophobic core of ODMB-SDS mixed micelles *via* its poly(propylene oxide) (PPO) block, which reduces the g value to between 1/3 and 1/2 due to the low V_H/V_L value of F127, thereby facilitating the formation of cylindrical SDS/ODMB/F127 mixed micelles. From the perspective of MOF crystallization, the soft matter phase transition of micellar structures can be elucidated through the charge density matching theory. According to charge density matching theory, changes in the surfactant head-group area (A) can significantly influence the micellar curvature and induce soft matter mesophase transitions.[36,37] Moreover, the charge density ρ_ε of the precursor within the mesopore wall is mutually shielded by the charges on the surfactant head group, and its average surface charge density is $1/A$, which can be described by eqn (2)

$$\rho_\varepsilon = \frac{1}{A} \quad (2)$$

where ρ_ε represents the charge density of the precursor within the mesopore wall and A is the head-group area of surfactants. As the charge density of the precursor varies during the

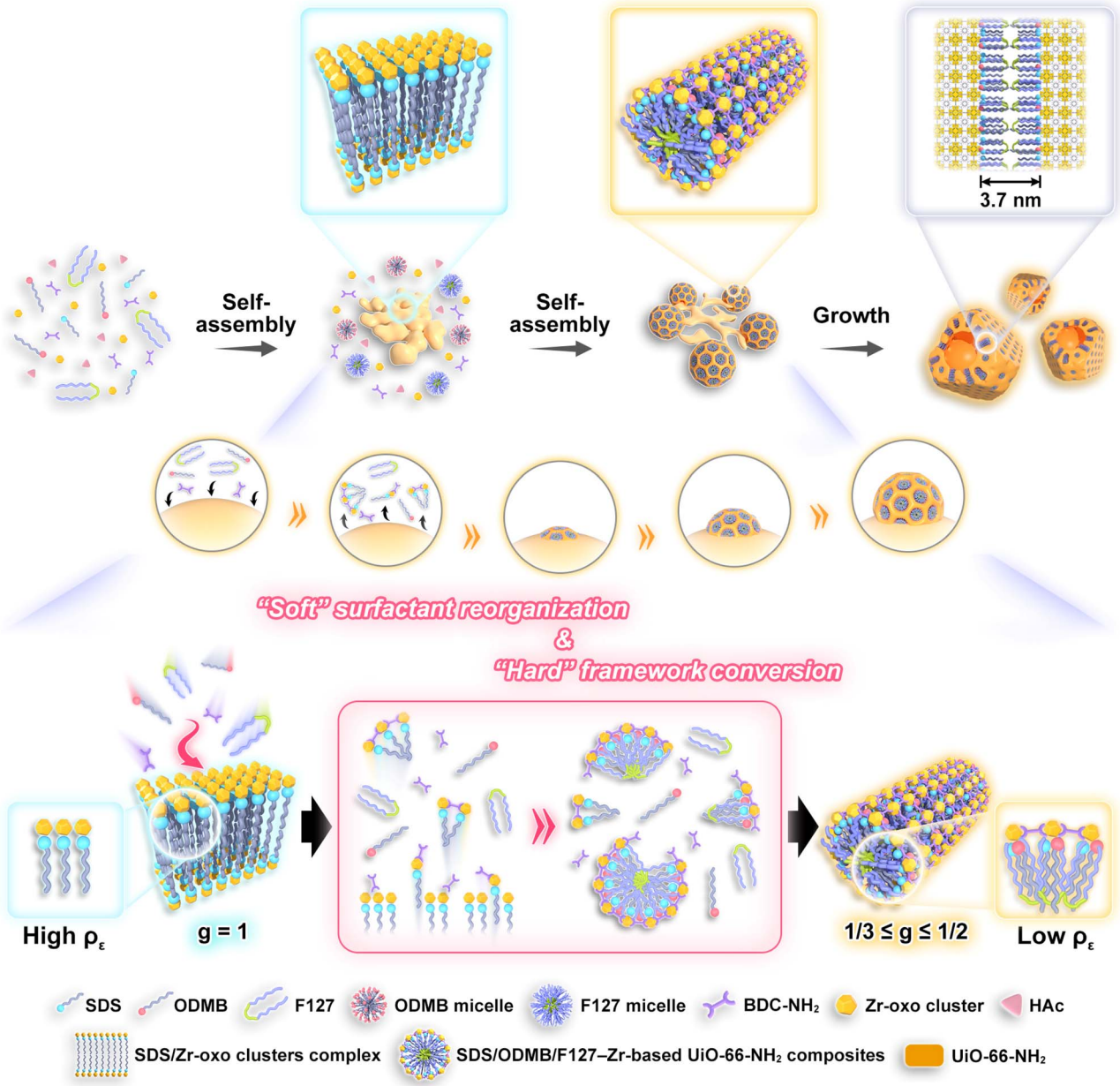

Fig. 3 Bioinspired mineralization mechanism for UiO-66-NH_2 mesoNBs. The formation of amorphous metastable SDS/Zr-oxo cluster complexes and their induced interface anisotropic assembly to crystalline UiO-66-NH_2 mesoNBs.

reaction, the corresponding A dynamically adjusts, leading to a mesophase transformation. Specifically, in the initial stage of synthesis, the high charge density of Zr-oxo clusters promotes a smaller A, favoring the formation of a lamellar surfactant configuration. As negatively charged BDC-NH_2 inserts between positively charged Zr-oxo clusters and MOF polymerization advances, the positive charge of the Zr-oxo clusters is partially neutralized and the distance between them increases, decreasing the density of Zr-oxo clusters. This causes A to increase and reduces the number of surfactants interacting with Zr-oxo clusters. Consequently, the micelle structure transitions from a tightly packed lamellar phase with low interfacial curvature to a more loosely packed cylindrical phase with higher interfacial curvature as the density of Zr-oxo clusters decreases. Under the synergistic effect of surfactant reorganization and MOF crystallization, the assembly of SDS/ODMB/F127 mixed micelles with UiO-66-NH_2 precursors accelerates the decomposition of SDS/Zr-oxo cluster complexes, ultimately directing the formation of mesoporous UiO-66-NH_2. Specifically, a structural transition of soft micelles occurs from a lamellar to a cylindrical phase, while the hard framework transforms from amorphous non-crosslinked Zr-oxo clusters to crystalline UiO-66-NH_2, simultaneously accompanied by a morphological transformation from coral-like to bowl-shaped nanostructures. This process closely resembles biomineralization, where flexible organic templates direct mineral deposition and facilitate

the formation of controlled porous structures.[21] Simultaneously, an amorphous metastable intermediate (calcium phosphate, calcium carbonate, *etc.*) initially forms and subsequently undergoes decomposition and reorganization, gradually transforming into crystals with hierarchical structures, such as those found in corals and bones.

Structure tailoring of the mesostructured UiO-66-NH_2

Building upon the outlined growth mechanism, we investigated the structural alterations of UiO-66-NH_2 nanoparticles by precisely tuning the assembly kinetics through adjusting the mass ratio of the three surfactants in the reaction system. The amount of SDS incorporated is expected to influence the size of the nucleated SDS/Zr-oxo cluster complexes. Adjusting the ratio of the anionic surfactant SDS to the surfactant ODMB affects their electrostatic interactions, which, in turn, impacts the nanostructure of the SDS/Zr-oxo cluster complexes and ultimately alters the final nano- and pore structure of UiO-66-NH_2. The morphological evolution of the UiO-66-NH_2 nanostructures is illustrated in Fig. 4. To understand this evolutionary process, TEM and SEM characterization studies were performed to analyze the mesoporous UiO-66-NH_2 products fabricated under different conditions. By simply adjusting the SDS/ODMB/F127 mass ratio in the reaction system from 0.11 : 0.18 : 0.71 to 0.24 : 0.38 : 0.38, and then to 0.25 : 0.60 : 0.15, the MOF particles can be continuously tuned from hierarchical hollow particles with mesoNBs as subunits (Fig. 4b and c) to bowl-like mesoporous particles with radially oriented mesochannels (Fig. 4e and f), and then to bowl-like mesoporous particles with a few cracks located near the bowl opening (Fig. 4h and i). The change in the mesoporous UiO-66-NH_2 nanostructure depends strongly on the shape of the generated SDS/Zr-oxo cluster complexes. When small amounts of SDS and ODMB are introduced into the reaction system (SDS/ODMB/F127 = 0.11 : 0.18 : 0.71), the SDS/Zr-oxo cluster complexes nucleate nanospheres with a diameter of approximately 100 nm (Fig. 4a, S12a and c). Mesostructured UiO-66-NH_2 nanocrystals agglomerate on the spherical SDS/Zr-oxo cluster complexes to form hierarchical

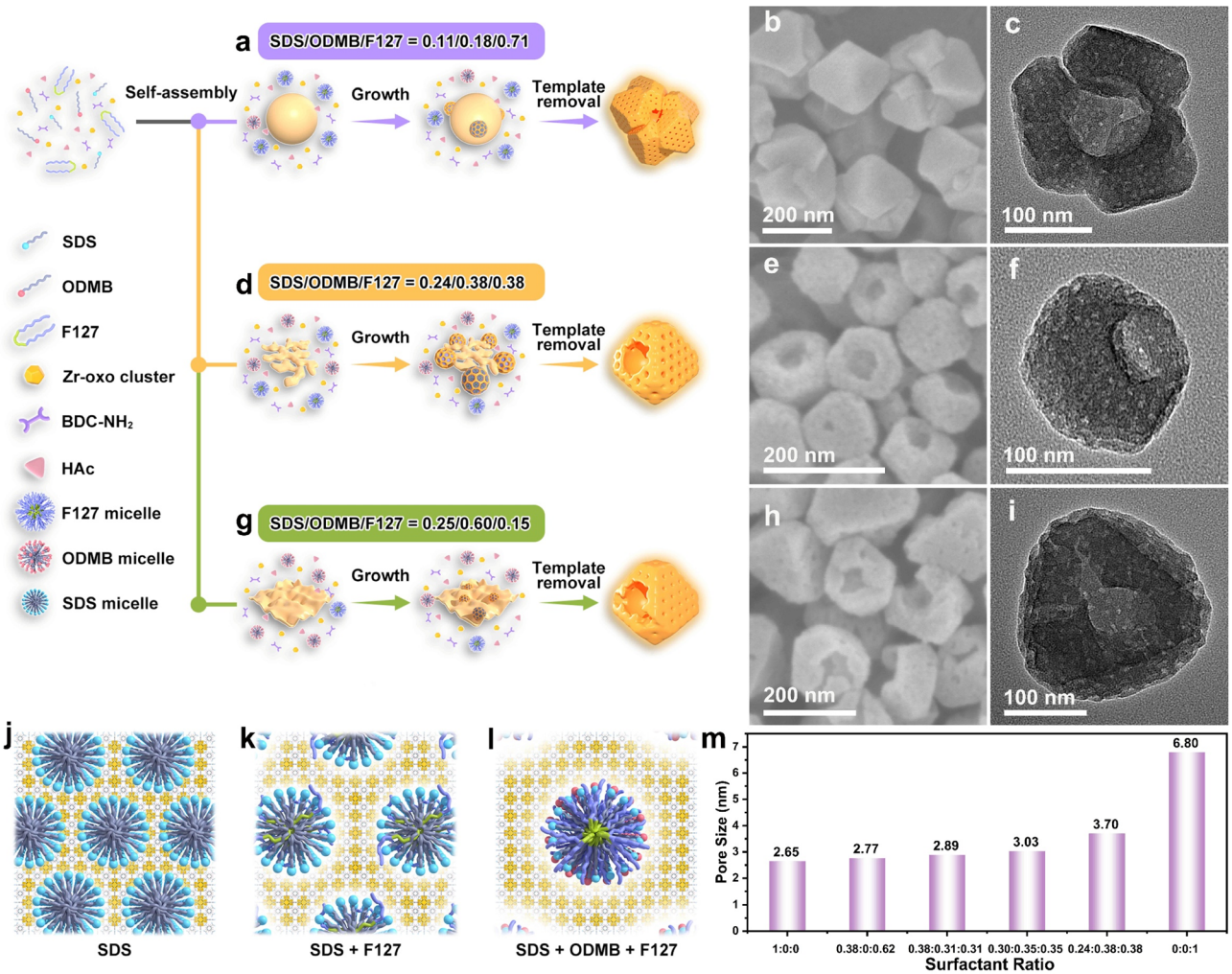

Fig. 4 Nanostructure and pore size regulations of mesostructured UiO-66-NH_2. Schematic illustration of the formation processes, SEM, and TEM images of (a–c) hollow UiO-66-NH_2 mesoNB aggregates, (d–f) UiO-66-NH_2 mesoNBs, (g–i), and UiO-66-NH_2 mesoNBs with cracks. 3D models of the (j) SDS micelles, (k) mixed micelles composed of SDS and F127, and (l) mixed micelles composed of SDS, ODMB, and F127 in the MOF matrix. (m) pore sizes of mesostructured UiO-66-NH_2 prepared at different SDS/ODMB/F127 ratios.

hollow particles with mesoNBs as subunits. Increasing the amounts of SDS and ODMB in equal proportions (SDS/ODMB/F127 = 0.24 : 0.38 : 0.38) results in larger SDS/Zr-oxo cluster complexes, which aggregate to form coral-like nanostructures (Fig. 4d and S4). Numerous coral-like SDS/Zr-oxo cluster complexes enable the uniform dispersion of UiO-66-NH_2 nucleation sites on their surfaces, resulting in well-dispersed UiO-66-NH_2 mesoNBs. Further increasing the amount of ODMB adjusts the SDS/ODMB ratio from 1 : 1.6 to 1 : 2.4 (SDS/ODMB/F127 = 0.25 : 0.60 : 0.15), promoting electrostatic neutralization between the positively charged cationic ODMB and the negatively charged anionic SDS. This reduction in electrostatic repulsion facilitates the aggregation of the SDS/Zr-oxo cluster complexes into wrinkled uneven sheet-like structures (Fig. 4g, S12b and d).[38] The raised portions of the flake-like SDS/Zr-oxo cluster complexes form the bowl opening, while the wrinkled regions create cracks at the edge of the bowl opening, resulting in some bowl-shaped mesoporous particles with a few cracks near the opening. These regulations deepen our understanding of how biomimetic mineralization processes employ amorphous precursors to control the nanostructures of crystalline materials. The XRD patterns in Fig. S13 exhibit characteristic reflections associated with the UiO-66-NH_2 framework across all nanostructures. Moreover, by precisely regulating the ratio of surfactants, the pore size of mesoporous UiO-66-NH_2 can be finely controlled. In the case of a reaction system that employs SDS as a soft template (Fig. 4j), the pore size of the resulting bowl-shaped UiO-66-NH_2 is 2.65 nm (Fig. S8 and S14). The introduction of both SDS and F127 to form binary micelles (Fig. 4k) facilitates an increase in pore size to 2.77 nm (Fig. S7 and S14). The incorporation of ODMB as a bridge connecting SDS and F127 allows for the formation of ternary micelles (Fig. 4l), which can achieve a pore size of 3.70 nm (Fig. 1d and S15). Moreover, precise adjustment of the SDS concentration can further finely tune the pore size of UiO-66-NH_2 mesoNBs. For instance, increasing the SDS concentration by 1.5 times reduces the pore diameter to 3.03 nm, while doubling the original SDS concentration decreases the pore diameter to 2.89 nm (Fig. 4m and S14). When UiO-66-NH_2 is prepared with only the F127 template, the mesopore size of the UiO-66-NH_2 particles can be extended to ~6.80 nm (Fig. S14 and S15). This understanding facilitates the design and preparation of mesoporous MOFs with precisely tailored small mesopore sizes, which show significant potential in applications such as catalysis,[39] drug delivery,[40] and separation processes.[41]

Application of the UiO-66-NH_2 mesoNB-derived electrocatalysts for the ORR

The asymmetric nanostructures and highly open pore architectures may enable UiO-66-NH_2 mesoNBs or their derived materials to fully utilize their internal matrix for catalytic reactions. To demonstrate the potential advantages of their derived carbon-based materials in ORR electrocatalysis, Fe–N–C mesoNBs are fabricated using a simple and efficient CVD method (Fig. 5a). In this conversion process, $FeCl_3$ molecules are vaporized and trapped in the mesopores of UiO-66-NH_2 mesoNBs, which are then pyrolyzed to form N-doped carbon with Fe–N sites, along with Fe and ZrO_2 nanoparticles, resulting in ZrO_2/Fe NPs & Fe–N–C mesoNBs (Fig. S16 and S17). Fe–N–C mesoNBs are produced after etching the Fe and inert ZrO_2 nanoparticles using HF solution. The SEM image (Fig. 5b) shows that the resultant Fe–N–C mesoNBs retain the bowl-like morphology. TEM images (Fig. 5c and d) show that the bowl-shaped carbon particles preserve the radially oriented pore structure after the pyrolysis treatment. Elemental mapping images depict the homogeneous distribution of Fe, N, and C elements in the bowl-like particles (Fig. 5e). Given their open bowl-like architecture and the locally accessible mesochannels, Fe–N–C mesoNBs with exposed active sites and enhanced diffusion are expected to be an ideal ORR electrocatalytic reactor. To investigate the structural and compositional advantages of Fe–N–C mesoNBs for ORR activity, we employ symmetric iron/nitrogen-doped carbon particles (Fe–N–C particles) synthesized by pyrolysis of UiO-66-NH_2 microCs and nitrogen-doped carbon mesoporous nanobowls (N–C mesoNBs) prepared by direct pyrolysis of UiO-66-NH_2 mesoNBs without adding an Fe source as control samples. SEM images reveal that both Fe–N–C particles (Fig. 5f and S18a) and N–C mesoNBs (Fig. S19a and d) maintain their original morphology after pyrolysis and HF etching. TEM images (Fig. 5g and h) reveal numerous mesopores in Fe–N–C particles. This is primarily because the thermally unstable ligand (BDC-NH_2) is easily removed during the pyrolysis process.[42] The highly symmetrical morphology and closed micropores of UiO-66-NH_2 microCs make their internal structure more vulnerable to stress accumulation from ligand decomposition, leading to the formation of internal mesopores. In contrast, the asymmetric nanostructure and open mesopores of UIO-66-NH_2 mesoNBs promote more efficient stress relief, which in turn reduces the possibility of internal framework damage.[43] Furthermore, the elemental mapping images (Fig. 5i) show that Fe, N, and C elements are homogeneously distributed within the whole particle.

The XRD patterns of Fe–N–C mesoNBs, Fe–N–C particles, and N–C mesoNBs exhibit a broad diffraction peak at 26° (Fig. S20), corresponding to the (002) crystalline plane of graphitic carbon. The Raman spectra of the three samples exhibit distinct D bands and G bands (Fig. 5j and S21), corresponding to defective carbon and graphite carbon, respectively. Among them, Fe–N–C mesoNBs exhibit a relatively higher I_D/I_G value of 0.93 compared to Fe–N–C particles and N–C mesoNBs, indicating a greater abundance of defects, which could enhance the adsorption of oxygen and other intermediates during the ORR.[44] X-ray photoelectron spectroscopy (XPS) is utilized to verify the composition and surface chemical states of catalysts. The full XPS survey spectra (Fig. S22 and S23) reveal the presence of C, N, Fe, O, and residual Zr in Fe–N–C mesoNBs and Fe–N–C particles. The high-resolution N 1s XPS spectra of Fe–N–C mesoNBs and Fe–N–C particles (Fig. 5k) can be deconvoluted into five peaks, corresponding to pyridinic N (398.7 eV), Fe–N_x (399.7 eV), pyrrolic N (400.6 eV), graphitic N (401.5 eV), and oxidized N (402.4 eV), while the spectrum of N–C mesoNBs (Fig. S24) lacks the peak of Fe–N_x, which is commonly regarded

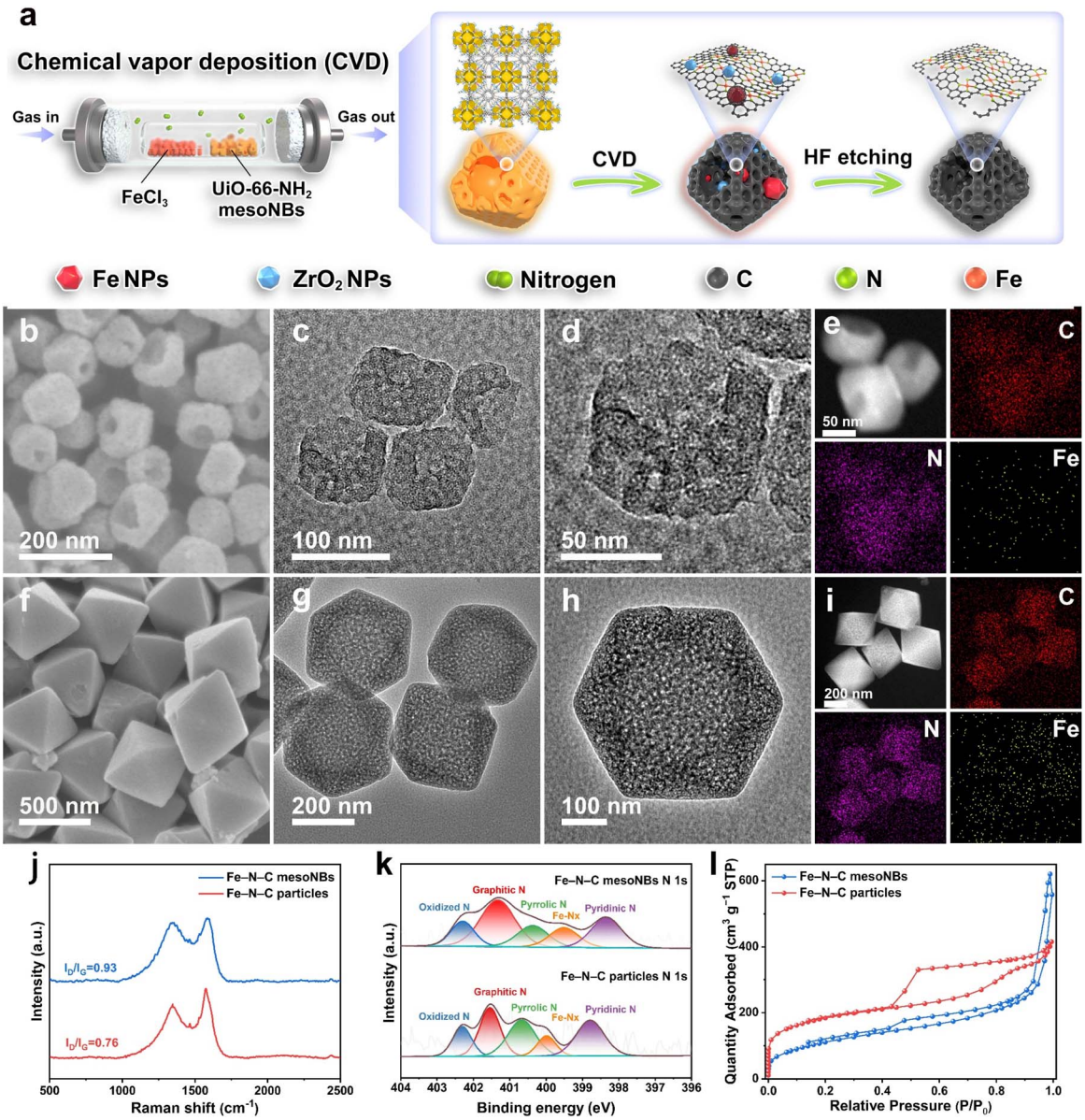

Fig. 5 Characterization of the UiO-66-NH_2-derived Fe–N–C mesoNBs and Fe–N–C particles. (a) Schematic illustration of the synthesis of Fe–N–C mesoNBs. SEM, TEM, and STEM images, and the corresponding EDS elemental mapping images of (b–e) Fe–N–C mesoNBs and (f–i) Fe–N–C particles. (j) Raman spectra, (k) high-resolution N 1s XPS spectra, and (l) N_2 sorption isotherms of Fe–N–C mesoNBs and Fe–N–C particles.

as the most efficient active site for oxygen electrocatalysis and has high selectivity for catalyzing the four-electron ORR pathway. The nitrogen sorption isotherms of Fe–N–C mesoNBs and Fe–N–C particles are shown in Fig. 5l. The H_2 hysteresis loop observed in the isotherms of Fe–N–C particles reflects a pore-blocking effect associated with ink-bottle pores featuring narrow necks and limited pore network connectivity. The H_3 hysteresis loop in the isotherms of Fe–N–C mesoNBs suggests the presence of mesopores. In contrast, the relatively narrow hysteresis loop throughout the pressure range indicates that there is no significant delay between the capillary evaporation and condensation for nitrogen gas, confirming the relatively open nature of the mesopores. Such an open mesoporous structure of Fe–N–C mesoNBs is anticipated to enhance mass transport and boost the utilization of active sites during the ORR. The comparable elemental compositions observed in the two samples suggest a similar concentration of active sites, which further substantiates that the improved catalytic performance can be attributed to the significantly promoted mass transfer facilitated by the mesoporous bowl-shaped nanoarchitecture of the Fe–N–C mesoNB catalysts (Table S2). Subsequently, the surface chemical properties of the materials were characterized. As illustrated in Fig. S25, the measured contact angles for the Fe–N–C mesoNBs and Fe–N–C particles are respectively 117° and 131°, demonstrating the hydrophobicity of the catalyst surface. These hydrophobic surfaces are conducive to the ORR process because they could facilitate the trap and diffusion of oxygen, thereby favoring the formation of

more triple-phase interfaces in alkaline electrolytes.[45] Additionally, the Fe–N–C mesoNBs present a smaller zeta potential compared with Fe–N–C particles (Fig. S26), suggesting a relatively weaker electrostatic interaction between OH^- anions and Fe–N–C mesoNB catalysts, which is favorable for the dissociation of OH^- from the three-phase reaction interface.[46]

Next, the ORR performances of the catalysts are assessed in an O_2-saturated 0.1 M KOH electrolyte utilizing a standard three-electrode system. The ORR activity of Fe–N–C mesoNBs synthesized by calcination at different temperatures ranging from 800 to 1100 °C is first assessed, among which Fe–N–C mesoNBs produced at 900 °C exhibit the highest activity (Fig. S27–S30). The linear sweep voltammetry (LSV) curves of Fe–N–C mesoNBs demonstrate a half-wave potential ($E_{1/2}$) of 0.89 V and a limiting current density (J_L) of 5.44 mA cm^{-2}, which are higher than those of the other control samples (Fig. 6a and b) and surpass those of most Fe-based catalysts documented in the literature (Table S3). Fe–N–C mesoNBs display a significantly smaller Tafel slope of 64.6 mV dec^{-1} compared to Fe–N–C particles (96.8 mV dec^{-1}), N–C mesoNBs (78.6 mV dec^{-1}), and Pt/C (77.4 mV dec^{-1}), as shown in Fig. 6c, which indicates a favorable ORR kinetic process for Fe–N–C mesoNBs. The rotating ring disk electrode (RRDE) measurements reveal an H_2O_2 yield below 9.3% with an average electron transfer number (n) of 3.89 (Fig. 6d). This is consistent with the results obtained from the Koutecky–Levich (K–L) plots (Fig. S31), indicating that Fe–N–C mesoNBs have high selectivity for direct four-electron transfer. The long-term stability of Fe–N–C mesoNBs is further examined through a voltammetric test. The LSV curve of Fe–N–C mesoNBs remains almost unchanged after over 5000 cycles (Fig. 6e). The TEM analysis (Fig. S32) of the Fe–N–C mesoNBs after the durability test reveals a well-retained morphology, demonstrating the excellent structural stability of Fe–N–C mesoNBs. Furthermore, Fe–N–C mesoNBs also exhibit superior tolerance to methanol crossover compared to Pt/C (Fig. 6f).

Finite element simulation for analyzing mass transfer behavior

To further elucidate why Fe–N–C mesoNBs exhibit enhanced electrocatalytic performance, a comparative finite element analysis is conducted to investigate the mass transfer behaviors

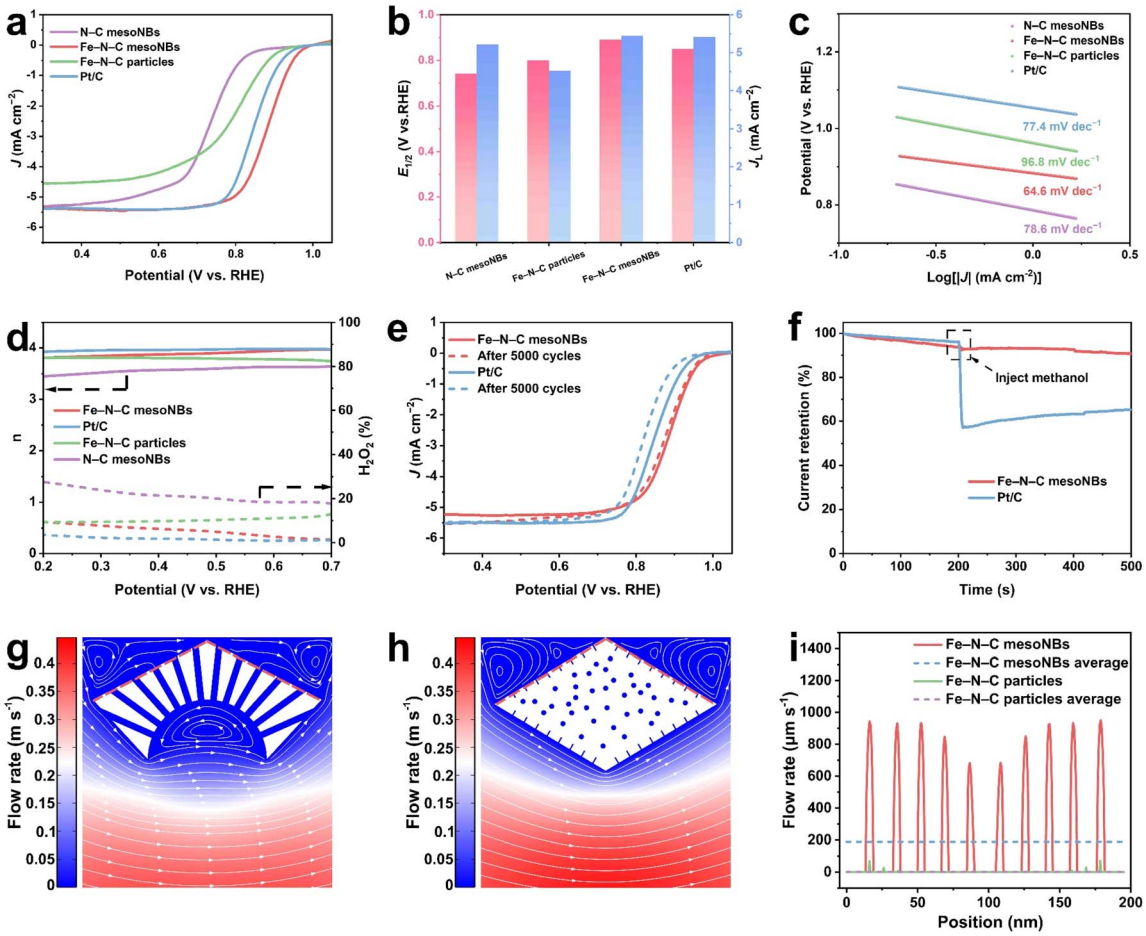

Fig. 6 Electrochemical tests of the Fe–N–C mesoNBs in 0.1 M KOH. (a) LSV curves, (b) $E_{1/2}$ and J_L, (c) the corresponding Tafel plots, and (d) electron transfer number and H_2O_2 yield of Fe–N–C mesoNBs, Fe–N–C particles, N–C mesoNBs, and Pt/C. (e) LSV curves of Fe–N–C mesoNBs and Pt/C before and after 5000 CV cycles. (f) Methanol tolerance test of Fe–N–C mesoNBs and Pt/C at 0.5 V_{RHE} with a rotation rate of 1600 rpm. The simulated velocity field of (g) Fe–N–C mesoNBs and (h) Fe–N–C particles. (i) Flow rate comparison of Fe–N–C mesoNBs and Fe–N–C particles along the specified path marked by the red dashed lines in Fig. 6g and h.

of Fe–N–C mesoNBs and Fe–N–C particles. Two models are constructed to represent the structural differences between Fe–N–C mesoNBs and Fe–N–C particles, with the particles positioned at the upper boundary of the calculated domain to represent their adhesion to the electrode. The simulated fluid velocity fields (Fig. 6g and h) and the associated flow rates along specified paths (Fig. 6i) demonstrate that the models' structural characteristics and pore sizes significantly influence the simulated electrolyte flow rate. For Fe–N–C mesoNBs, velocity field simulation (Fig. 6g) reveals a large vortex forming within the bowl and two small vortices forming in the gap between the Fe–N–C mesoNBs and the upper boundary of the calculated domain, likely induced by localized backflow from fluid impacting the bowl surface.[47] These vortices form a low-pressure area in their central region because the rotational motion of the fluid consumes some of its kinetic energy, thereby causing a drop in local pressure.[48] This leads to a pressure difference around the vortex and drives the electrolyte to flow toward the center of the vortex. Given the larger pressure difference across the large vortex compared to the small vortex and the highly open mesoporous structure of Fe–N–C mesoNBs, the electrocatalysts exhibit significant fluid acceleration within the mesochannels. In comparison, only two vortices are generated in the gap between the Fe–N–C particles and the upper boundary of the calculated domain (Fig. 6h). However, the closed surface micropores of Fe–N–C particles restrict mass transport, leading to a significant reduction in the flow rate within the channels. The flow velocity for the two models is compared in Fig. 6i to examine the mass transport ability in detail. Fe–N–C mesoNBs present a velocity of 188.885 μm s^{-1}, which is approximately 265 times faster than that of Fe–N–C particles (0.713 μm s^{-1}). This highlights the pivotal role of carefully engineered bowl-shaped nanostructures and mesoporous channels in optimizing electrocatalytic performance. A mesoporous carbon bowl featuring abundant exposed active sites and enhanced nanodiffusion properties could be an optimal catalytic platform for the ORR, facilitating rapid O_2 transport and timely expulsion of the generated H_2O during the electrochemical reaction.

Conclusions

In conclusion, based on a biomineralization approach, a novel soft/hard matter phase transition co-mediated assembly strategy has been developed to fabricate anisotropic UiO-66-NH_2 mesoNBs with precisely tunable pore size. The key to this strategy is that the strong coordination between SDS surfactants and Zr-oxo clusters facilitates the precise construction of metastable amorphous SDS/Zr-oxo cluster complexes with a lamellar mesophase, followed by the dissolution–conversion of the amorphous complexes and the heterogeneous nucleation and anisotropic assembly of mesostructured SDS/ODMB/F127-MOF nanounits on their surface to generate bowl-shaped hierarchically porous MOF nanoarchitectures with cylindrical mesochannels. Changes in the packing parameters caused by the assembly of different surfactants into mixed "soft" micelles and variations in the charge density of "hard" frameworks during crystallization from amorphous non-crosslinked Zr-oxo clusters to a crystalline MOF matrix are crucial driving forces in changing the micellar curvature and inducing mesophase transition. Moreover, by adjusting the feed ratio of the three surfactants, the shapes of amorphous SDS/Zr-oxo cluster complexes can be facilely manipulated to generate diverse nanostructured UiO-66-NH_2, such as hollow mesoporous particles with mesoNBs as subunits and mesoporous bowls with cracks near the opening, and enable the precise and continuous modulation of pore sizes ranging from 2.65 to 6.80 nm. To demonstrate their potential application, the UiO-66-NH_2 mesoNBs undergo CVD followed by etching to transform into Fe–N–C mesoNBs, which function as efficient ORR electrocatalysts with a half-wave potential of 0.89 V. Finite element simulation results show that this unique bowl-shaped mesoporous structure greatly promotes the mass transfer process, compared with catalysts derived from traditional microporous MOFs with symmetrical morphologies. Our work not only provides new insights into a potential mechanism of MOF biomimetic mineralization but also offers a promising strategy for controlling complex pathways to precisely fabricate anisotropic hierarchically porous MOFs with high structural tunability.

Author contributions

Conceptualization: R. S, J. H, and B. G. Synthesis: R. S. and J. H. Investigation: R. S. J. H, X. C., and B. Z. Analysis: R. S, B. L, G. C, H. X, B. W, and Y. G. Funding acquisition: B. G. and S. Z. Supervision: B. G. Writing—original draft: R. S and B. G. writing—review and editing: R. S, X. C., B. G, and Y. Y.

Conflicts of interest

There are no conflicts to declare.

Data availability

All the data supporting this article have been included in the main text and the supplementary informarion (SI). Supplementary information: detailed characterizations and synthesis of UiO-66-NH_2 mesoNBs and additional results and data (PDF). See DOI: https://doi.org/10.1039/d5sc06744h.

Acknowledgements

We thank the National Natural Science Foundation of China (Grant 22375071, 22288101, 21920102005, and 21835002), the National Key Research and Development Program of China (Grant 2021YFA1501202), and the 111 Project (B17020) for supporting this work. Y. Y. thanks the JST-ERATO Materials Space-Tectonics Project (JPMJER2003), the ARC Australian Laureate Fellowship (FL230100095), and the Queensland node of the NCRIS-enabled Australian National Fabrication Facility (ANFF). We acknowledge the use of English editing software, such as Grammarly and ChatGPT, for checking grammatical errors in our manuscript.

Notes and references

1 Z. Yang, Y. Belmabkhout, L. N. McHugh, D. Ao, Y. Sun, S. Li, Z. Qiao, T. D. Bennett, M. D. Guiver and C. Zhong, *Nat. Mater.*, 2023, **22**, 888–894.
2 N. Tyagi, Y. H. Wijesundara, J. J. Gassensmith and A. Popat, *Nat. Rev. Mater.*, 2023, **8**, 701–703.
3 G. Cai, P. Yan, L. Zhang, H.-C. Zhou and H.-L. Jiang, *Chem. Rev.*, 2021, **121**, 12278–12326.
4 L.-H. Xu, S.-H. Li, H. Mao, Y. Li, A.-S. Zhang, S. Wang, W.-M. Liu, J. Lv, T. Wang, W.-W. Cai, L. Sang, W.-W. Xie, C. Pei, Z.-Z. Li, Y.-N. Feng and Z.-P. Zhao, *Science*, 2022, **378**, 308–313.
5 B. E. R. Snyder, A. B. Turkiewicz, H. Furukawa, M. V. Paley, E. O. Velasquez, M. N. Dods and J. R. Long, *Nature*, 2023, **613**, 287–291.
6 T. Chen, K. Yu, C. Dong, X. Yuan, X. Gong, J. Lian, X. Cao, M. Li, L. Zhou, B. Hu, R. He, W. Zhu and X. Wang, *Coord. Chem. Rev.*, 2022, **467**, 214615.
7 S.-C. Qi, X.-Y. Qian, Q.-X. He, K.-J. Miao, Y. Jiang, P. Tan, X.-Q. Liu and L.-B. Sun, *Angew. Chem., Int. Ed.*, 2019, **58**, 10104–10109.
8 M. K. Albolkany, C. Liu, Y. Wang, C.-H. Chen, C. Zhu, X. Chen and B. Liu, *Angew. Chem., Int. Ed.*, 2021, **60**, 14601–14608.
9 Z. Lv, R. Lin, Y. Yang, K. Lan, C.-T. Hung, P. Zhang, J. Wang, W. Zhou, Z. Zhao, Z. Wang, J. Zou, T. Wang, T. Zhao, Y. Xu, D. Chao, W. Tan, B. Yan, Q. Li, D. Zhao and X. Li, *Nat. Chem.*, 2025, **17**, 177–185.
10 S. Bi, H. Banda, M. Chen, L. Niu, M. Chen, T. Wu, J. Wang, R. Wang, J. Feng, T. Chen, M. Dincă, A. A. Kornyshev and G. Feng, *Nat. Mater.*, 2020, **19**, 552–558.
11 H. Xu, J. Han, B. Zhao, R. Sun, G. Zhong, G. Chen, Y. Yamauchi and B. Guan, *Nat. Commun.*, 2023, **14**, 8062.
12 L. Peng, H. Peng, L. Xu, B. Wang, K. Lan, T. Zhao, R. Che, W. Li and D. Zhao, *J. Am. Chem. Soc.*, 2022, **144**, 15754–15763.
13 J. Han, H. Xu, B. Zhao, R. Sun, G. Chen, T. Wu, G. Zhong, Y. Gao, S. L. Zhang, Y. Yamauchi and B. Guan, *J. Am. Chem. Soc.*, 2024, **146**, 18979–18988.
14 T. Wu, G. Chen, J. Han, R. Sun, B. Zhao, G. Zhong, Y. Yamauchi and B. Guan, *J. Am. Chem. Soc.*, 2023, **145**, 16498–16507.
15 R. Wang, K. Lan, Z. Chen, X. Zhang, C.-T. Hung, W. Zhang, C. Wang, S. Wang, A. Chen, W. Li, X. Xu and D. Zhao, *Matter*, 2019, **1**, 1274–1284.
16 T. Zhao, L. Chen, M. Liu, R. Lin, W. Cai, C.-T. Hung, S. Wang, L. Duan, F. Zhang, A. Elzatahry, X. Li and D. Zhao, *Nat. Chem.*, 2023, **15**, 832–840.
17 M. Wu, Z. Shao, N. Zhao, R. Zhang, G. Yuan, L. Tian, Z. Zhang, W. Gao and H. Bai, *Science*, 2023, **382**, 1379–1383.
18 Z. Zhang, X. Yang, P. Li, Y. Wang, X. Zhao, J. Safaei, H. Tian, D. Zhou, B. Li, F. Kang and G. Wang, *Adv. Mater.*, 2022, **34**, 2206970.
19 F. Chen, H. Huang, F. Zhang, R. Wang, L. Wang, Z. Chang, L. Cao, W. Zhang, L. Li, M. Chen, D. Shao, C. Yang, W.-f. Dong and W. Sun, *Adv. Mater.*, 2025, **37**, 2413385.
20 X. Wu, K. Yu, Y. He, X. Cao, T. Chen and W. Zhu, *Inorg. Chem.*, 2024, **63**, 24141–24149.
21 R. Zhao and E. Amstad, *Small*, 2025, **21**, 2401052.
22 A. Gal, R. Wirth, J. Kopka, P. Fratzl, D. Faivre and A. Scheffel, *Science*, 2016, **353**, 590–593.
23 F. C. Meldrum and H. Cölfen, *Chem. Rev.*, 2008, **108**, 4332–4432.
24 S. A. Davis, S. L. Burkett, N. H. Mendelson and S. Mann, *Nature*, 1997, **385**, 420–423.
25 I. A. Aksay, M. Trau, S. Manne, I. Honma, N. Yao, L. Zhou, P. Fenter, P. M. Eisenberger and S. M. Gruner, *Science*, 1996, **273**, 892–898.
26 P. T. Tanev and T. J. Pinnavaia, *Science*, 1996, **271**, 1267–1269.
27 W. L. Noorduin, A. Grinthal, L. Mahadevan and J. Aizenberg, *Science*, 2013, **340**, 832–837.
28 G. Cai and H.-L. Jiang, *Angew. Chem., Int. Ed.*, 2017, **56**, 563–567.
29 K. Li, J. Yang, R. Huang, S. Lin and J. Gu, *Angew. Chem., Int. Ed.*, 2020, **59**, 14124–14128.
30 T.-T. Chen, J.-T. Yi, Y.-Y. Zhao and X. Chu, *J. Am. Chem. Soc.*, 2018, **140**, 9912–9920.
31 A. F. Ogata, A. M. Rakowski, B. P. Carpenter, D. A. Fishman, J. G. Merham, P. J. Hurst and J. P. Patterson, *J. Am. Chem. Soc.*, 2020, **142**, 1433–1442.
32 V. T. Kelleppan, J. P. King, C. S. G. Butler, A. P. Williams, K. L. Tuck and R. F. Tabor, *Adv. Colloid Interface Sci.*, 2021, **297**, 102528.
33 A. A. McLachlan and D. G. Marangoni, *J. Colloid Interface Sci.*, 2006, **295**, 243–248.
34 Y.-Q. Yeh, B.-C. Chen, H.-P. Lin and C.-Y. Tang, *Langmuir*, 2006, **22**, 6–9.
35 L. Peng, H. R. Peng, Y. Liu, X. Wang, C. T. Hung, Z. W. Zhao, G. Chen, W. Li, L. Q. Mai and D. Y. Zhao, *Sci. Adv.*, 2021, **7**, eabi7403.
36 A. Monnier, F. Schüth, Q. Huo, D. Kumar, D. Margolese, R. S. Maxwell, G. D. Stucky, M. Krishnamurty, P. Petroff, A. Firouzi, M. Janicke and B. F. Chmelka, *Science*, 1993, **261**, 1299–1303.
37 R. Kumar Parsapur, A. M. Hengne, G. Melinte, O. Refa Koseoglu, R. P. Hodgkins, A. Bendjeriou-Sedjerari, Z. Lai and K.-W. Huang, *Angew. Chem., Int. Ed.*, 2024, **63**, e202314217.
38 W. Zhang, B. Li, Y.-G. Sun, A.-M. Cao and L.-J. Wan, *J. Am. Chem. Soc.*, 2020, **142**, 17897–17902.
39 Z. Jiang, X. Xu, Y. Ma, H. S. Cho, D. Ding, C. Wang, J. Wu, P. Oleynikov, M. Jia, J. Cheng, Y. Zhou, O. Terasaki, T. Peng, L. Zan and H. Deng, *Nature*, 2020, **586**, 549–554.
40 Y. Chen, P. Li, J. A. Modica, R. J. Drout and O. K. Farha, *J. Am. Chem. Soc.*, 2018, **140**, 5678–5681.
41 J.-R. Li, J. Sculley and H.-C. Zhou, *Chem. Rev.*, 2012, **112**, 869–932.

42 R. Xu, Q. Ji, P. Zhao, M. Jian, C. Xiang, C. Hu, G. Zhang, C. Tang, R. Liu, X. Zhang and J. Qu, *J. Mater. Chem. A*, 2020, **8**, 7870–7879.
43 J. Chu, W. Wang, Q. Yu, C.-Y. Lao, L. Zhang, K. Xi, K. Han, L. Xing, L. Song, M. Wang and Y. Bao, *J. Mater. Chem. A*, 2020, **8**, 779–788.
44 O. L. Li, S. Chiba, Y. Wada, G. Panomsuwan and T. Ishizaki, *J. Mater. Chem. A*, 2017, **5**, 2073–2082.
45 S. Liu, Z. Cao, Y. Meng, Y. Li, W. Yang, Z. Chang, W. Liu and X. Sun, *ACS Appl. Mater. Interfaces*, 2021, **13**, 26853–26860.
46 W.-B. Tu, L.-N. Song, S. Liang, Y. Wang, Y. Sun, H.-F. Wang and J.-J. Xu, *Adv. Energy Mater.*, 2025, **15**, 2404946.
47 A. A. Gossler and J. S. Marshall, *J. Fluid Mech.*, 2001, **431**, 371–405.
48 L. Jiang, W. Wang, Y. Shi, J. Chen, L. Bai and L. Zhou, *Phys. Fluids*, 2025, **37**, 025164.